ACS Sustainable Chemistry & Engineering
pubs.acs.org/journal/ascecg
Research Article

Cadmium-Sacrifice Mediated Vacancy Engineering on Manganese Phosphide for Enhancing Oxygen Reduction and Zn-Air Batteries

Zuyang Luo,[§] Xue Shao,[§] Jinshan Cheng, Jiayin Xie, Baofa Liu, Fengli Wei, Tayirjan Taylor Isimjan,* Jingya Guo,* and Xiulin Yang*

Cite This: ACS Sustainable Chem. Eng. 2025, 13, 18018−18026
Read Online

ABSTRACT: Exploiting the efficiency and durability of oxygen reduction reaction (ORR) electrocatalysts for Zn-air batteries (ZABs) remains a tremendous challenge. In this work, a novel sacrificial agent strategy was employed to construct vacancy-rich MnP/$Mn_{5.64}P_3$ heterostructure nanobicrystals on nitrogen-doped carbon (Mn_xP_y/NC). Multiple *ex/in situ* characterizations reveal that the Cd sacrificial agent induces structural reconstruction and vacancy generation, which accelerates electron transfer, optimizes the transformation of intermediates, and suppresses the production of byproducts. As a result, the optimized Mn_xP_y/NC catalyst shows remarkable ORR activity, with an onset potential of 0.93 V and a limited current density of 5.6 mA cm^{-2}. Notably, Mn_xP_y/NC-based aqueous ZABs exhibit an impressive power density (135.9 mW cm^{-2}) and an ultralong cycle life (600 h), and the corresponding flexible device demonstrates excellent mechanical stability. This work presents a strategy for designing highly active transition metal phosphide-based catalysts using the sacrificial agent toward the ORR.

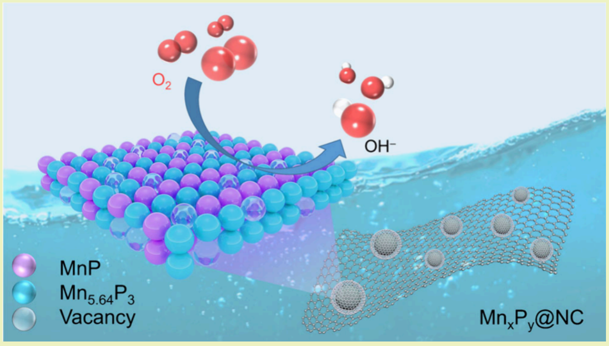

KEYWORDS: *Transition metal phosphide, Heterostructure; Vacancy engineering, Oxygen reduction, Zn-air battery*

INTRODUCTION

Zn-air batteries (ZABs) are considered to be promising devices for energy storage and conversion due to their high energy density and eco-friendly nature.[1−3] To improve the competitiveness and efficiency of ZABs, several issues must be addressed. The major one is to improve the kinetics of the oxygen reduction reaction (ORR) in the air cathode discharge process.[4,5] Conventionally, Pt-based materials (PBMs) are the benchmark catalysts for ORR, but the implementation is hampered by issues such as natural scarcity, poor durability, and susceptibility to byproducts.[6,7] Therefore, it is crucial to advance cost-effective alternatives for PBMs that can achieve high efficiency and a long lifespan for ZAB technology.

Recently, there has been exploration of various non-noble metal-based catalysts with potential applications, including 3*d* transition metal-based carbides,[8] nitrides,[9] oxides,[10] and phosphides.[11] Among these, transition metal phosphides (TMPs) have garnered intensive attention owing to their unique electron configuration, multifunctional active sites, and affordability.[12] However, there is still a lack of comprehensive understanding of the effect of TMPs on ORR and the underlying reaction mechanism, which motivates further research enthusiasm.[13] Universally, phosphorus (P) possesses abundant valence electrons, which can induce delocalized charge state density, thereby ultimately optimizing metal sites electron configuration.[14] Noticeably, the lone pair of electrons on the 3*p* orbitals of P can interact with the 3*d* orbitals of transition metals to endow large-scale charge density differences, favoring oxygen adsorption and subsequent *OOH desorption during ORR.[15] Compared with other transition metals (Fe, Co, and Cu), Mn-based materials can offer unique advantages in the ORR process due to their weak reactivity with the Fenton reaction.[16] Furthermore, Mn-based materials reveal low toxicity and long life spans in electrochemistry reactions.[17] Unfortunately, relevant research on Mn-based ORR electrocatalysts is still in infancy due to their unsatisfactory activity.[18] Therefore, various modification methods, such as architectural strategies,[19] interface engineering,[20] and vacancy regulation,[21] have been proposed to enhance the performance of Mn-based phosphides. Nonetheless, conventional routes have not significantly improved the ORR activity of Mn-based catalysts.

Here, we utilized Cd as a sacrificial agent to synthesize the MnP/$Mn_{5.64}P_3$ heterostructure electrocatalyst (Mn_xP_y/NC). The optimized Mn_xP_y/NC exhibited excellent four-electron

Received: July 3, 2025
Revised: September 25, 2025
Accepted: September 26, 2025
Published: October 13, 2025

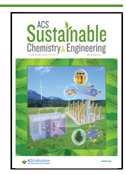

https://doi.org/10.1021/acssuschemeng.5c06704
ACS Sustainable Chem. Eng. 2025, 13, 18018−18026

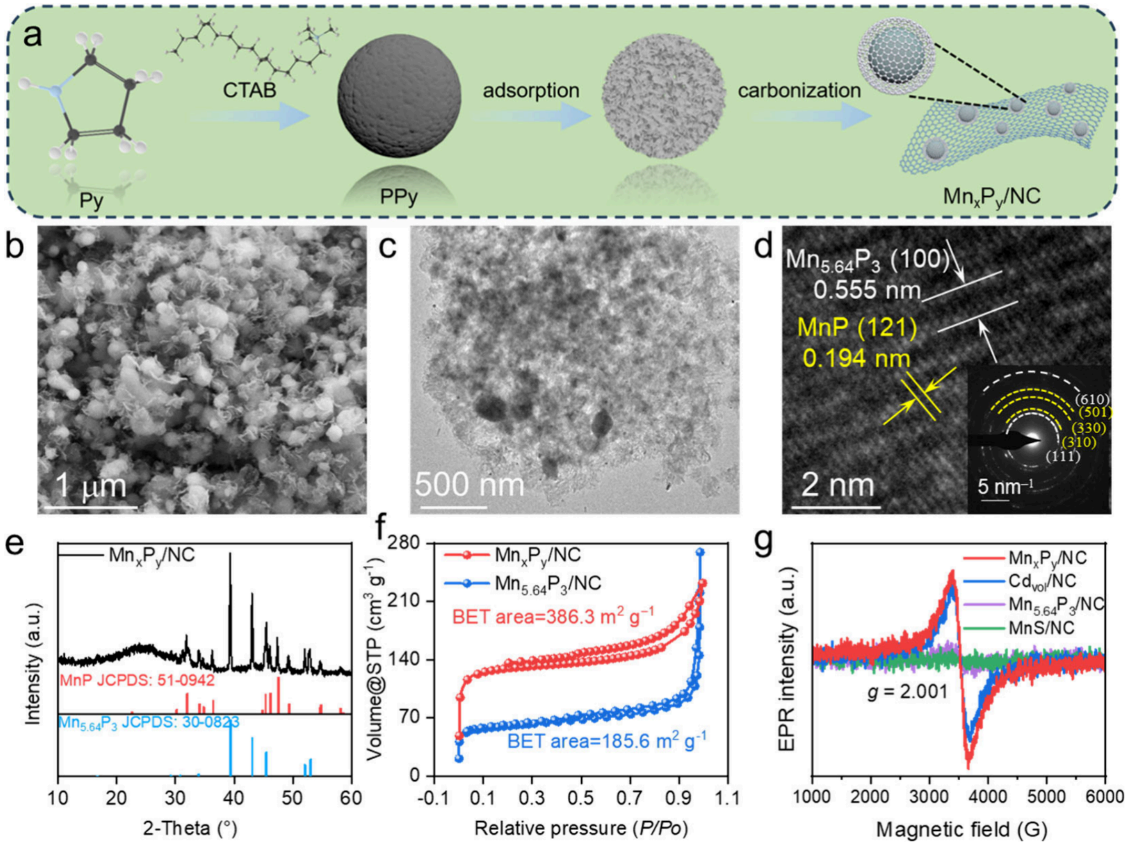

Figure 1. (a) The synthetic procedure of Mn_xP_y/NC. (b) SEM image, (c) TEM image, and (d) HRTEM image (inset: SAED pattern). (e) XRD pattern of Mn_xP_y/NC. (f) N_2 adsorption/desorption isotherms of Mn_xP_y/NC and $Mn_{5.64}P_3$/NC. (g) EPR spectra.

ORR activity with a limited current density (j_L) of 5.6 mA cm^{-2} and an onset potential (E_{onset}) of 0.93 V. Such high activity can be attributed to the strong coupling effect between vacancy engineering and the MnP/$Mn_{5.64}P_3$ heterostructure. *In-situ* techniques confirm that this strong coupling effect not only promotes the fast conversion of intermediates but also suppresses the generation of H_2O_2. Furthermore, the aqueous Mn_xP_y/NC-based ZAB exhibits high power density (135.9 mW cm^{-2}) and maintains stable charge−discharge cycling for over 600 h. The flexible ZAB assembled with catalyst displays substantial power density (50.2 mW cm^{-2}), surpassing that of the one assembled with Pt/C (1.25 V and 42.8 mW cm^{-2}), demonstrating promising potential for practical applications.

RESULTS AND DISCUSSION

Figure 1a illustrates the detailed synthesis procedure of Mn_xP_y/NC. Typically, pyrrole (Py) monomers are polymerized as polypyrrole nanospheres (PPy) with surface clusters (Figure S1a), in which hexadecyl trimethylammonium bromide (CTAB) acts as a surfactant and ammonium persulfate (APS) acts as an oxidizing agent. Subsequently, Cd and Mn ions are loaded onto these formed PPy nanoparticle surfaces (Figure S1b). Ultimately, the metal-supported nanospheres are calcined with red phosphorus at a high temperature to form heterogeneous Mn_xP_y/NC. As profiled in Figure 1b and c, SEM and TEM images of Mn_xP_y/NC identified a definite three-dimensional (3D) interconnected nitrogen-doped carbon network loading with nanospheres, which not only provides more shortcuts for mass transport but also ensures the stability of active centers in the alkaline environment.[22] The high-resolution TEM (HRTEM) image of Mn_xP_y/NC reveals a lattice spacing of 0.194 nm corresponding to the (121) plane of $Mn_{5.64}P_3$ and 0.555 nm consistent with the (100) plane of MnP (Figure 1d). Additionally, the selected area electron diffraction (SAED) pattern reaffirmed the coexistence of (610), (501), (330), (310) and (111) crystal planes for Mn_xP_y/NC and further revealed a polycrystalline structure (insets of Figure 1d). Inductively coupled plasma mass spectrometry (ICP-MS) detected 33.73 wt % Mn element but no Cd element in Mn_xP_y/NC (Table S1), indicating that the Cd element has completely evaporated during the high-temperature pyrolysis process (Cd boiling point: 765 °C). The crystal phase of the Mn_xP_y/NC composite is analyzed by an X-ray diffraction (XRD) pattern, which showed typical crystal structure peaks of MnP (JCPDS: 51−0942) and $Mn_{5.64}P_3$ (JCPDS: 30−0823) (Figure 1e), indicating that the composite is composed of two different manganese phosphide components. A series of control experiments are performed, while products can match well with $Mn_{5.64}P_3$ (JCPDS: 30−0823), MnP (JCPDS: 51−0942) and MnS (JCPDS: 06−0518), respectively (Figure S2). It is worth noting that the formation of MnS is due to the addition of APS. It is evident that the Cd sacrifice induces structural reconstruction to form MnP/$Mn_{5.64}P_3$ heterostructure.[23] The specific surface area and pore size distribution of the catalysts were characterized by N_2 adsorption−desorption isotherms, as shown in Figure S3 and S4. The isotherms of all samples exhibit a type IV characteristic, indicating a typical mesoporous structure. The Brunauer−Emmett−Teller (BET) specific surface area of Mn_xP_y/NC, $Mn_{5.64}P_3$/NC, and Cd_{vol}/NC is

https://doi.org/10.1021/acssuschemeng.5c06704
ACS Sustainable Chem. Eng. 2025, 13, 18018−18026

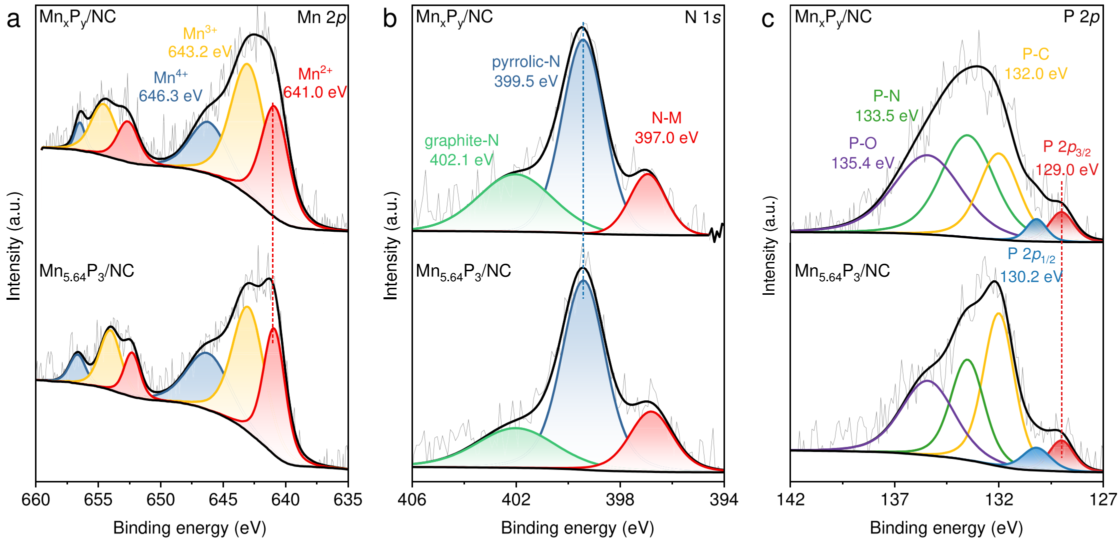

Figure 2. High-resolution XPS spectra of (a) Mn 2*p*, (b) P 2*p*, and (c) N 1*s* for Mn_xP_y/NC and $Mn_{5.64}P_3$/NC, respectively.

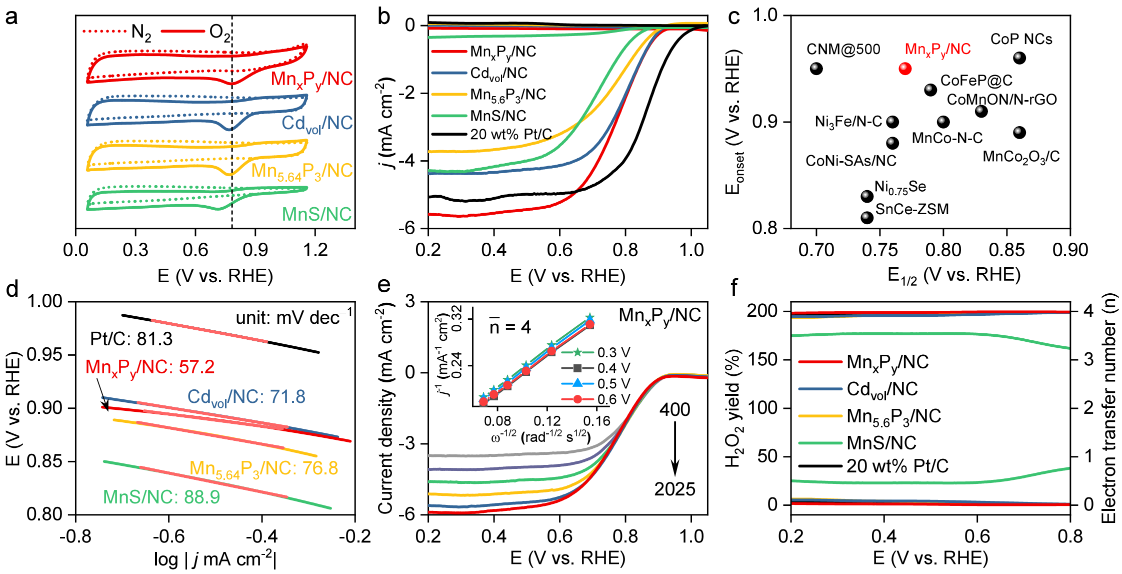

Figure 3. (a) CV curves in N_2 or O_2-saturated 0.1 M KOH. (b) LSV curves with a rotation speed of 1600 rpm. (c) Comparison of $E_{1/2}$ and E_{onset} of Mn_xP_y/NC with other advanced catalysts. (d) Tafel slope plots. (e) LSV curves of Mn_xP_y/NC with different rotation speeds of 400−2025 rpm (inset: K-L plots at different potentials). (f) H_2O_2 yields and transfer electron numbers.

386.3, 185.6, and 382.3 m^2 g^{-1}, respectively. The pore size of the samples was analyzed by the Barret−Joyner−Halenda (BJH) method. It can be observed that the average pore diameter decreases significantly from 128.1 nm ($Mn_{5.64}P_3$/NC) to 3.8 nm (Cd_{vol}/NC) and 3.7 nm (Mn_xP_y/NC). The substantial increase in specific surface area, combined with the reduction in pore size for Mn_xP_y/NC, provides an ideal space for anchoring active sites and enhancing mass transfer. The Raman spectra of different catalysts showed D (1345 cm^{-1}) and G (1590 cm^{-1}) bands of carbon, corresponding to disordered carbon and graphitic carbon, respectively.[24] The higher I_D/I_G band intensity ratio of Mn_xP_y/NC (1.19) than NC (1.17), $Mn_{5.64}P_3$/NC (1.11), and MnS/NC (1.09) indicates ample disordered carbon is generated after pyrolysis at 1000 °C (Figure S5). Typically, disordered carbon partially reflects defects in the substrate, which is considered to be an active substance which can significantly improve the oxygen redox kinetics.[25] Electron paramagnetic resonance (EPR) spectroscopy serves as a powerful tool for vacancy characterization. As shown in Figure 1g, the characteristic signal at g = 2.001 corresponds to vacancies on the materials.[26] Notably, the EPR signal intensity in Mn_xP_y/NC is obviously higher than that in $Mn_{5.64}P_3$/NC, indicating that Cd evaporation leads to a significant increase in the number of vacancies.

X-ray photoelectron spectroscopy (XPS) was employed to gain detailed chemical state information. The survey spectrum of Mn_xP_y/NC confirmed the presence of Mn, P, N, and C, but the absence of Cd, which is consistent with the ICP results (Figure S6a). The C 1*s* XPS spectrum of Mn_xP_y/NC was deconvoluted into four components, including C═O (288.5 eV), C−O (286.0 eV), C−C/C−N (284.8 eV), and C═C (284.0 eV), serving as a calibration standard (Figure S6b).[27] The Mn 2*p* XPS spectrum of Mn_xP_y/NC and $Mn_{5.64}P_3$/NC showed three major binding energies at 646.3, 643.2, and 641.0 eV, corresponding to Mn^{4+}, Mn^{3+}, and Mn^{2+}, respectively (Figure 2a).[28] Notably, there exists a higher proportion of

https://doi.org/10.1021/acssuschemeng.5c06704
ACS Sustainable Chem. Eng. 2025, 13, 18018−18026

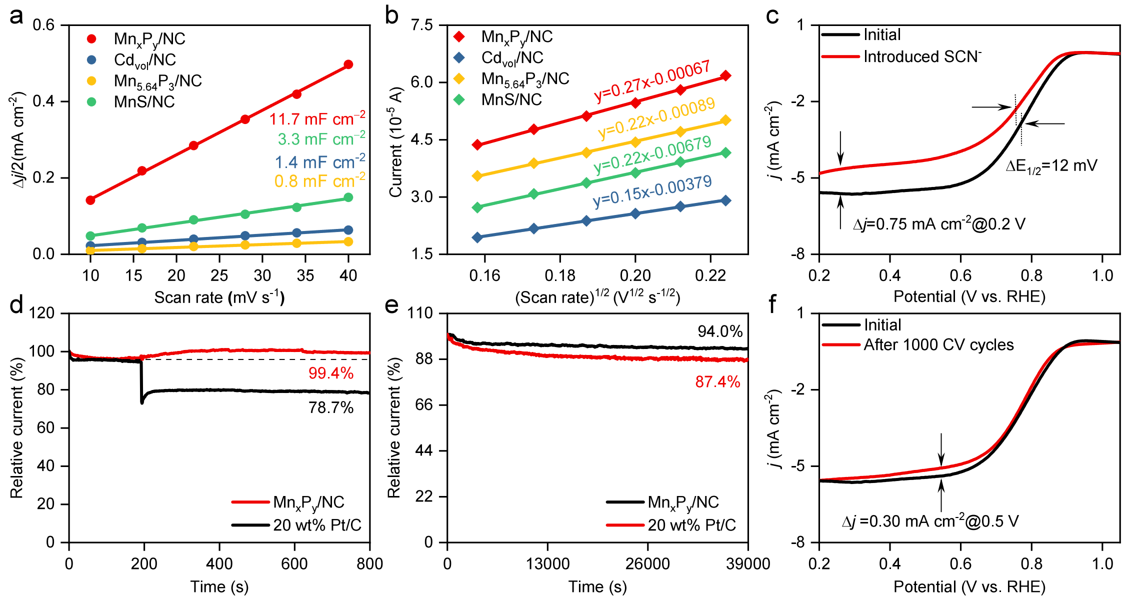

Figure 4. (a) Electrochemical double layer capacitance and (b) CV fitting curves in 0.1 M KCl containing a 5 mM $K_3[Fe(CN)_6]$ solution. (c) LSV curves of Mn_xP_y/NC before and after KSCN. (d) Methanol tolerance test. (e) Chronoamperometric (CP) responses for Mn_xP_y/NC and Pt/C. (f) LSV curves of Mn_xP_y/NC before and after 1000 CV cycles.

Mn^{3+} in Mn_xP_y/NC (51.5%) than $Mn_{5.64}P_3$/NC (43.7%), which can contribute to the ORR process according to previous literature.[29] There is no significant peak in the XPS spectrum of Cd, confirming its absence in the sample and no function during the electrocatalysis process (Figure S6c). In Figure 2b, the peaks at 132.0, 133.5, and 135.4 eV are attributed to P−C, P−N and P−O species, respectively, implying partial P atoms were incorporated into carbon.[30−32] The presence of the P−O bond can be attributed to oxygen adsorption on the phosphorus surface, which suggests that the material has a strong interaction with the oxygen-containing intermediate.[33] Furthermore, peaks at binding energies of 129.0 and 130.2 eV are attributed to $2p_{1/2}$ and $2p_{3/2}$ of P species, certifying the formation of phosphide.[34] The N 1*s* spectra of two samples showed three peaks at 400.5, 398.4, and 396.1 eV, corresponding to graphitic-N, pyrrolic-N, and pyridinic-N, respectively (Figure 2c).[35,36] Obviously, there are more pyrrolic-N and pyridinic-N in Mn_xP_y/NC (55% and 21%) than in $Mn_{5.64}P_3$/NC (45% and 20%). According to the elemental analysis results, the total N content in Mn_xP_y/NC is 2.04 wt %, significantly higher than that in $Mn_{5.64}P_3$/NC (1.59 wt%) (Table S2). Previous research indicates that the augmentation of N content, specifically the ratio of pyrrolic-N and pyridinic-N, has the potential to regulate the electron/spin state density of the material.[37] Furthermore, the presence of pyridinic-N is indispensable for initiating the initial electron transfer and activating the neighboring atoms during the ORR process.[38]

The ORR electrochemical performance was tested by using the standard three-electrode system. To convert the measured potential to RHE, we systematically conducted the experimental calibration of the reference electrode against RHE (Figure S7, S8 and Table S3).[39] All catalysts were uniformly deposited on the electrode surface to minimize errors during testing (Figure S9).[40] The optimized calcination temperature and the corresponding performance parameters are presented in Figure S10, where the best catalyst was obtained at an annealing temperature of 1000 °C. In Figure 3a, a more positive oxygen redox peak at 0.8 V was observed in the O_2-saturated 0.1 M KOH solution, indicating promising ORR activity of Mn_xP_y/NC.[41] Meanwhile, the Mn_xP_y/NC exhibited excellent performance in linear sweep voltammetry (LSV) curves ($E_{1/2}$ = 0.77 V, E_{onset} = 0.93 V, j_L = 5.6 mA cm^{-2}@0.2 V), which was superior to $Mn_{5.64}P_3$/NC ($E_{1/2}$ = 0.71 V, E_{onset} = 0.90 V, j_L= 3.7 mA cm^{-2}@0.2 V), Cd_{vol}/NC ($E_{1/2}$ = 0.77 V, E_{onset} = 0.92 V, j_L= 4.4 mA cm^{-2}@0.2 V) and MnP ($E_{1/2}$ = 0.64 V, E_{onset} = 0.78 V, j_L= 2.8 mA cm^{-2}@0.2 V) (Figure 3b and S11). Furthermore, the excellent ORR activity of the Mn_xP_y/NC can be compared with that of Pt/C ($E_{1/2}$ = 0.85 V, E_{onset} = 0.90 V, j_L= 5.18 mA cm^{-2}@0.2 V) and previous catalysts (Figure 3c and Table S4). Typically, a larger j_L indicates more favorable mass transfer characteristics, while the theoretical limiting current density is approximately 6 mA cm^{-2}. The observed deviation may arise from differences between practical and theoretical conditions, as well as variations in the mass transfer efficiency of catalysts toward O_2.[42] Meanwhile, a more positive E_{onset} indicates a quicker electron transfer rate, while a higher $E_{1/2}$ indicates a stronger intrinsic activity.[43] Furthermore, the Tafel slopes of Mn_xP_y/NC, NC, $Mn_{5.64}P_3$/NC, and Pt/C were calculated from the LSV curves and used to analyze the ORR catalytic kinetics. The Tafel slope plots in Figure 3d follow the sequence: Mn_xP_y/NC (57.2 mV dec^{-1}) < Cd_{vol}/NC (71.8 mV dec^{-1}) < $Mn_{5.64}P_3$/NC (76.8 mV dec^{-1}) < Pt/C (81.3 mV dec^{-1}) < MnS/NC (88.9 mV dec^{-1}). A smaller Tafel slope indicates faster ORR kinetics for the Mn_xP_y/NC catalyst. Its Tafel slope differs from reported values for the typical 2 + 2e$^-$ ORR pathway, and its LSV curve lacks the two-plateau characteristic of this mechanism. Thus, the Mn_xP_y/NC catalyst primarily follows the 4e$^-$ ORR pathway. The enhanced electrochemical performance can be attributed to the beneficial interfacial coupling effect and increased vacancy induced by Cd sacrifice, which modulate the electronic structure of the catalyst to optimize the adsorption−desorption equilibrium of reaction intermediates. The Koutecky−Levich (K-L) equation is used to analyze the kinetic parameters of ORR on the catalyst surface. In

https://doi.org/10.1021/acssuschemeng.5c06704
ACS Sustainable Chem. Eng. 2025, 13, 18018−18026

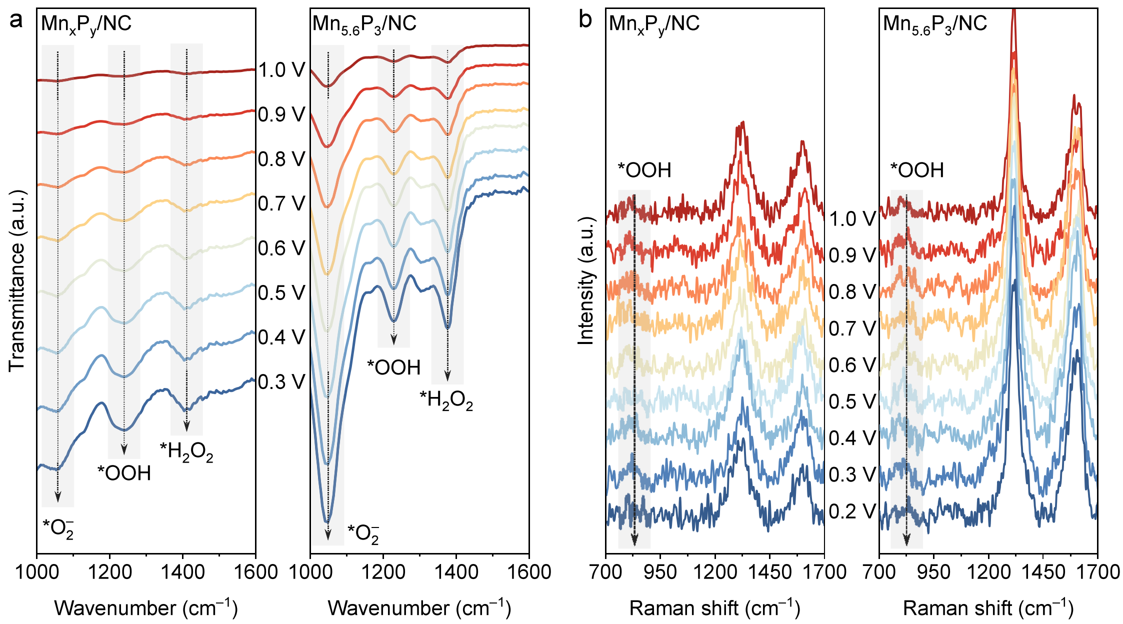

Figure 5. (a) *In-situ* FTIR collected on Mn_xP_y/NC (left) and $Mn_3P_{5.64}$/NC (right), and (b) *in-situ* Raman spectroscopy collected on Mn_xP_y/NC (left) and $Mn_3P_{5.64}$/NC (right) during ORR electrocatalysis.

agreement with the literature, the electron transfer number obtained from the K-L equation is close to 4 (Figure 3e, inset: K-L plot) after treating the current density for the 0.3−0.6 V potential interval, suggesting that Mn_xP_y/NC mainly follows the $4e^-$ ORR pathway.[44−48] Figure 3f provides further insight into the catalyst reaction route and calculated HO_2^- yield of ORR, where the HO_2^- yield is below 5%, and the average "*n*" value of Mn_xP_y/NC is close to 4, indicating a $4e^-$-dominated reaction pathway.

Electrochemical double layer capacitance (C_{dl}) was calculated by CV curves in the nonfaradaic potential range which is relevant to the electrochemically active surface area (ECSA) (Figure S12). Mn_xP_y/NC offers the highest C_{dl} of 11.7 mF cm^{-2}, indicating the most plentiful active sites, vastly superior to that of $Mn_{5.64}P_3$/NC (0.8 mF cm^{-2}) (Figure 4a). The linear relationship was obtained by CV test in a mixed solution of 5 mM $K_3[Fe(CN)_6]$ + 0.1 M KCl (Figure S13), and the electron transfer characteristics were evaluated by the Randles−Sevcik equation. The ECSA value of Mn_xP_y/NC is 0.73 m^2 g^{-1} (Figure 4b), being 1.24, 1.78, and 1.22 times greater than that of $Mn_{5.64}P_3$/NC (0.59 m^2 g^{-1}), NC (0.41 m^2 g^{-1}) and MnS/NC (0.60 m^2 g^{-1}), respectively. Generally, SCN^- featured a formidable affinity with metal ions, thus poisoning active centers smoothly.[10] The LSV curves of Mn_xP_y/NC before and after adding the KSCN solution revealed that $E_{1/2}$ declined by 12 mV and j_L by 0.75 mA cm^{-2}@0.2 V, which identifies Mn species acting as the major ORR active species (Figure 4c). Furthermore, the ORR activity appears to remain in the LSV curve obtained after reaction with SCN^-, which could be attributed to the presence of NC acting as a secondary active site in the oxygen reduction. The methanol tolerance test was executed by injecting 3.0 M methanol into the electrolyte during the CP course, and Mn_xP_y/NC exhibited a marvelous tolerance with a 99.4% retention rate, overmatching Pt/C (78.7%) (Figure 4d). The durability of the Mn_xP_y/NC was assessed by the CP curve, which retains 94% after 40000 s, while the Pt/C showed a poorer durability (87.4%), due to the agglomeration effect of Pt particles (Figure 4e).[49] Similarly, the $E_{1/2}$ of Mn_xP_y/NC was almost unchanged and j_L decreased by only 0.3 mA cm^{-2} at 0.5 V after 1000 cycles of CV scans, confirming its extraordinary stability (Figure 4f). The above results signify that Mn_xP_y/NC possesses a more admirable methanol tolerance and stability than Pt/C, certifying its potential practical application prospects in direct methanol fuel cells and metal−air batteries.

The vacancy engineering will influence the catalytic behavior of the active centers. An in-depth understanding of the oxygen reduction mechanism over the Mn active center would in turn guide the rational design of efficient metal-based phosphides. Herein, by combination with *in situ* Raman and *in situ* Fourier transform infrared spectroscopy (FTIR), the active reinforced mechanism of rich-vacancy Mn_xP_y/NC was unclosed.

In-situ FTIR spectra of both Mn_xP_y/NC and $Mn_3P_{5.64}$/NC were recorded between 1000 and 1600 cm^{-1} in the potential region from 1.0 to 0.3 V (vs RHE) (Figure 5a). For both catalysts, a distinct absorption peak located at ≈1112 cm^{-1} corresponds to the O−O stretching mode of adsorbed O_2 molecules.[50] The peak at 1212 cm^{-1} emerges and increases gradually with decreasing potentials, indicating the bending mode vibrations of adsorbed *OOH on the catalyst surface.[51] Additionally, the distinct peaks appeared at the band positions of ∼1312 cm^{-1}, attributed to surface-adsorbed hydroperoxide (*H_2O_2).[52] Notably, with the decrease of potentials, their intensities increase significantly in $Mn_3P_{5.64}$/NC, demonstrating the gradual accumulation of *O_2, *OOH and H_2O_2, and inevitable generation of byproduct H_2O_2. In contrast, these tendencies are not obvious in Mn_xP_y/NC, which indicates a strong catalytic capability of Mn_xP_y/NC for the conversion of intermediates (including *O_2 to *OOH and *OOH to *O). It is therefore reasonable to deduce that MnP facilitates O_2 adsorption and transformation of intermediates (*O_2 and *OOH), thus accelerating the oxygen reduction kinetics. *In-situ* Raman spectroscopy was further conducted to elucidate the transformation of *OOH during the ORR electrocatalysis (Figure 5b). A distinct Raman peak at ≈ 820 cm^{-1}, assigned to *OOH, was detected for both Mn_xP_y/NC and $Mn_3P_{5.64}$/NC,

https://doi.org/10.1021/acssuschemeng.5c06704
ACS Sustainable Chem. Eng. 2025, 13, 18018−18026

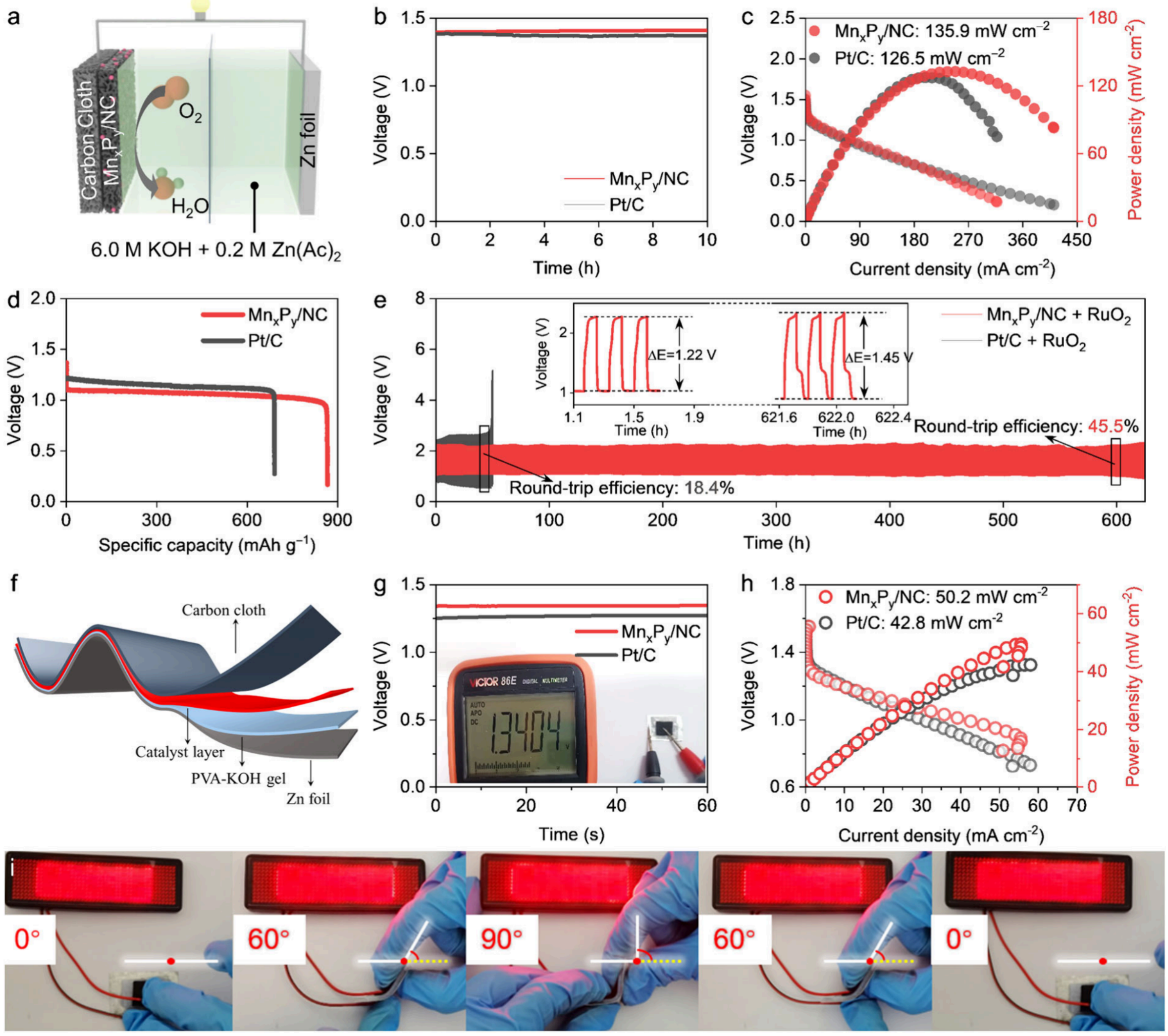

Figure 6. (a) Schematic configuration of the assembled ZAB. (b) OCV plots of Mn_xP_y/NC and 20 wt % Pt/C. (c) Discharge polarization curves and the corresponding power density curves. (d) Specific capacity plots. (e) Galvanostatic cycling at 5 mA cm^{-2} (inset: curves at the start and end of tests). (f) Configuration, (g) OCV plots, (h) discharge polarization curve, and corresponding power density curves of flexible solid-state ZAB. (i) Photos of the LED panel powered by flexible ZAB at different folding angles of 0°, 30°, 60°, 90°, and back to 0°.

and become increasingly pronounced as the applied potential decreases.[53] This Raman peak corresponding to *OOH species appeared at a lower potential (1.00 V) for Mn_xP_y/NC compared with that for $Mn_3P_{5.64}/NC$ (0.90 V), suggesting that the formation of *OOH is significantly accelerated on vacancy-rich Mn_xP_y/NC heterostructures. Additionally, this signal associated with *OOH disappears at 0.2 V for Mn_xP_y/NC, whereas $Mn_3P_{5.64}/NC$ exhibits a weak Raman signal. These phenomena indicate a faster conversion of *O_2 to *OOH and *OOH to *O on Mn_xP_y/NC during the ORR.

Encouraged by the robust ORR performance, we conducted ZAB tests using Mn_xP_y/NC as the air cathode (Figure 6a). The Mn_xP_y/NC-based ZAB demonstrated an OCV of 1.40 V, surpassing that of Pt/C (1.35 V) (Figure 6b). Moreover, Mn_xP_y/NC-based ZAB manifested a larger peak power density (135.9 mW cm^{-2}) than Pt/C (126.5 mW cm^{-2}) and recently reported materials (Figure 6c and Table S5). Figure 6d presents the specific capacity based on the normalized mass of the consumed Zn. The Mn_xP_y/NC-based ZAB has a specific capacity of 866.1 mAh g^{-1} (theoretical energy density: 1601.9 mWh g^{-1}), outperforming the commercial Pt/C-based ZAB (690.3 mAh g^{-1}, theoretical energy density: 1276.8 mWh g^{-1}). Due to the poor OER activity of the catalyst (Figure S14), and in order to make ZAB show good reversibility in the stability test, Mn_xP_y/NC + RuO_2 was mixed with a mass ratio of 1:1 as the air electrode. Figure 6e is the corresponding charge/discharge cycle curve of Mn_xP_y/NC-based ZAB, with an inset reflecting the voltage gap at the start and end. During initial cycles, the Mn_xP_y/NC-based ZAB exhibited charge and discharge voltages of 2.27 and 1.05 V, respectively, with a voltage gap of 1.22 V. Even after a charge−discharge cycle of more than 600 h, the voltage gap only increases by 0.21 V, demonstrating the ultralong stability for this device. In contrast, a Pt/C-based ZAB exhibits an excessively wider charge/discharge voltage over 70 h. Also, the round-trip efficiency remained at 45.5% even after the 600 h cycle. To explore the application of Mn_xP_y/NC in wearable devices, a solid-state flexible ZAB configuration was implemented (Figure 6f). The Mn_xP_y/NC-based flexible ZABs delivered an OCV of 1.34 V (Figure 6g) and a power density of 50.2 mW cm^{-2} (Figure 6h), which is superior to Pt/C (1.25 V and 42.8 mW cm^{-2}). As shown in Figure 6i, this flexible ZAB can

https://doi.org/10.1021/acssuschemeng.5c06704
ACS Sustainable Chem. Eng. 2025, 13, 18018−18026

smoothly illuminate the LED board while being bent at different angles (0°, 30°, 60°, and 90°), and the LED board remained lit when the flexible ZAB was bent back to 0°. The galvanostatic discharge curves show that the Mn_xP_y/NC + RuO_2-based flexible ZAB maintains a stable discharge for over 24 h (Figure S15). In contrast, the ZAB assembled with Pt/C + RuO_2 exhibits severe degradation after 20 h of operation, highlighting the superior structural stability of the Mn_xP_y/NC-based flexible ZAB. Overall, these findings demonstrate the potential of Mn_xP_y/NC for practical energy device applications ranging from conventional ZABs to flexible battery configurations.

Generally, the ORR mechanism (4e$^-$ pathway) consists of four primary stages: O_2 adsorption on active sites followed by protonation to form *OOH; cleavage of *OOH to generate adsorbed *O; protonation of *O to produce OH^-; desorption of OH^- from the catalyst surface.[54] The selectivity of an electrocatalyst for the ORR is determined by its interaction with the intermediate OOH*. A strong interaction with OOH* will lead to the breaking of the O−O bond, initiating a 4e$^-$ dominated reaction pathway.[55] Mn-based phosphides are known for their moderate adsorption strength for intermediates and inactivity toward the Fenton reaction, which optimizes the reaction process and promotes 4e$^-$ ORR route.[56] For instance, Dou et al. reported that Co_2P materials shifted the *d*-band center positively by approximately 1.72 eV compared to pristine Co, which facilitates the reaction of intermediates with active sites.[57] Similarly, Chao et al. introduced Mn into Co−M−C to synthesize MnCo−N−C and reduce the yield of H_2O_2 by about 15%.[58] Furthermore, a mass of research proves that constructing vacancies and coupling heterogeneous components are efficient tactics to improve electrocatalyst activity. Duan at al. reported that vacancies could weaken the hybridization of Ni 3*d* and P 2*p* orbitals, enriching the electron density of Ni and P atoms nearby the vacancy to facilitate the adsorption of active intermediate.[59] Kong et al. combined rich-N carbon with deficient-N carbon to optimize the electron cloud density at the interface, thus increasing the half-wave potential of the composite by 15%.[47]

Based on the above discussion, the extraordinary ORR activity and ZAB performance of the Mn_xP_y/NC catalyst can be attributed to the following factors. (1) High specific surface area and porous structure are beneficial to exposing active sites and facilitating mass transport. (2) The inactivity of Mn_xP_y toward the Fenton reaction can optimize the 4e$^-$ reaction route. (3) The vacancy-rich MnP/$Mn_{5.64}P_3$ heterostructure promotes electron transfer and intermediate transformation.

CONCLUSIONS

In summary, vacancy-rich Mn_xP_y/NC nanobicrystals were developed through a feasible Cd-sacrificial agent strategy for the oxygen reduction reaction (ORR) and Zn-air battery (ZAB). Experimental investigation confirmed the strong interaction between two manganese phosphides featuring abundant vacancies and a 3D interconnected network-supported nanosphere architecture, facilitating the transformation of intermediates and exposure of active sites. Hence, Mn_xP_y/NC exhibited 4e$^-$ selectivity and superior ORR activity. Furthermore, the catalyst-based ZAB demonstrated a higher peak power density than Pt/C. Moreover, the corresponding flexible device maintained a consistent voltage across varying bending angles (bent at 0, 45, and 90°), indicating its superior flexibility and wearability. This study presents an avenue for the rational design and construction of efficient catalysts for ZABs and other energy storage devices.

ASSOCIATED CONTENT

Supporting Information

The Supporting Information is available free of charge at https://pubs.acs.org/doi/10.1021/acssuschemeng.5c06704.

Experimental details, electrochemical measurements, SEM images, XRD patterns, BET data, XPS spectra, Raman spectra, ICP metal content, elemental analyzer information, electrochemical test data, catalyst deposition on RDE images, and ORR performance comparison (PDF)

AUTHOR INFORMATION

Corresponding Authors

Tayirjan Taylor Isimjan − *Saudi Arabia Basic Industries Corporation (SABIC) at King Abdullah University of Science and Technology (KAUST), Thuwal 23955-6900, Saudi Arabia*; Email: isimjant@sabic.com

Jingya Guo − *Guangxi Key Laboratory of Low Carbon Energy Materials, School of Chemistry and Pharmaceutical Sciences, Guangxi Normal University, Guilin 541004, China*; Email: jyguo@gxnu.edu.cn

Xiulin Yang − *Guangxi Key Laboratory of Low Carbon Energy Materials, School of Chemistry and Pharmaceutical Sciences, Guangxi Normal University, Guilin 541004, China*; orcid.org/0000-0003-2642-4963; Email: xlyang@gxnu.edu.cn

Authors

Zuyang Luo − *Guangxi Key Laboratory of Low Carbon Energy Materials, School of Chemistry and Pharmaceutical Sciences, Guangxi Normal University, Guilin 541004, China*

Xue Shao − *Guangxi Key Laboratory of Low Carbon Energy Materials, School of Chemistry and Pharmaceutical Sciences, Guangxi Normal University, Guilin 541004, China*

Jinshan Cheng − *Guangxi Key Laboratory of Low Carbon Energy Materials, School of Chemistry and Pharmaceutical Sciences, Guangxi Normal University, Guilin 541004, China*

Jiayin Xie − *Guangxi Key Laboratory of Low Carbon Energy Materials, School of Chemistry and Pharmaceutical Sciences, Guangxi Normal University, Guilin 541004, China*

Baofa Liu − *Guangxi Key Laboratory of Low Carbon Energy Materials, School of Chemistry and Pharmaceutical Sciences, Guangxi Normal University, Guilin 541004, China*

Fengli Wei − *Guangxi Key Laboratory of Low Carbon Energy Materials, School of Chemistry and Pharmaceutical Sciences, Guangxi Normal University, Guilin 541004, China*

Complete contact information is available at: https://pubs.acs.org/10.1021/acssuschemeng.5c06704

Author Contributions

[§]Z.L. and X.S. contributed equally to this work. The manuscript was written through contributions of all authors. All authors have given approval to the final version of the manuscript.

Notes

The authors declare no competing financial interest.

■ ACKNOWLEDGMENTS

This work has been supported by the National Natural Science Foundation of China (no. 52363028, 21965005), Natural Science Foundation of Guangxi Province (2021GXNSFAA076001), Guangxi Technology Base and Talent Subject (GUIKE AD23023004, GUIKE AD20297039).

■ REFERENCES

(1) Tang, T.; Jiang, W.-J.; Liu, X.-Z.; Deng, J.; Niu, S.; Wang, B.; Jin, S.-F.; Zhang, Q.; Gu, L.; Hu, J.-S.; Wan, L.-J. Metastable Rock Salt Oxide-Mediated Synthesis of High-Density Dual-Protected M@NC for Long-Life Rechargeable Zinc-Air Batteries with Record Power Density. *J. Am. Chem. Soc.* **2020**, *142*, 7116.

(2) Zhang, A.; Wu, J.; Xue, L.; Yan, S.; Zeng, S. Probing Heteroatomic Dopant-Activity Synergy over Co_3O_4/Doped Carbon Nanotube Electrocatalysts for Oxygen Reduction Reaction. *Inorg. Chem.* **2020**, *59*, 403.

(3) Li, Z.; Yao, Y.; Niu, Y.; Zhang, W. A.; Chen, B.; Zeng, X.; Zou, J. Multi-Heteroatom-Doped Hollow Carbon Tubes as Robust Electrocatalysts for the Oxygen Reduction Reaction, Oxygen and Hydrogen Evolution Reaction. *Chem. Eng. J.* **2021**, *418*, 129321.

(4) Liu, M.; Liu, Z.; Chen, W.; Liu, Z.; Li, Z.; Pi, X.; Du, Q.; Lai, X.; Xia, Y.; Li, Y. NiFe Nanoparticle-Encapsulated Ultrahigh-Oxygen-Doped Carbon Layers as Bifunctional Electrocatalysts for Rechargeable Zn-Air Batteries. *Inorg. Chem.* **2023**, *62*, 11199.

(5) Yao, Y.; Jiang, T.; Lim, S. Y.; Frandsen, C.; Li, Z.; Dou, Y.; Wu, F.; Qin, J.; Zou, J.; Stamate, E.; Zhang, W. Universal Synthesis of Half-Metallic Diatomic Catalysts for Efficient Oxygen Reduction Electrocatalysis. *Small* **2023**, *19*, 2304655.

(6) Li, Z.; Niu, W.; Yang, Z.; Zaman, N.; Samarakoon, W.; Wang, M.; Kara, A.; Lucero, M.; Vyas, M. V.; Cao, H.; Zhou, H.; Sterbinsky, G. E.; Feng, Z.; Du, Y.; Yang, Y. Stabilizing Atomic Pt with Trapped Interstitial F in Alloyed PtCo Nanosheets for High-Performance Zinc-Air Batteries. *Energy Environ. Sci.* **2020**, *13*, 884.

(7) Devi, B.; Bhardwaj, A.; Gambhir, D.; Roy, B.; Karmakar, A.; Dey, G.; Jain, A.; Mondal, B.; Koner, R. R. Cu(II)-Based Coordination Polymer as a Pristine Form Usable Electrocatalyst for Oxygen Reduction Reaction: Experimental Evaluation and Theoretical Insights into Biomimetic Mechanistic Aspects. *Inorg. Chem.* **2022**, *61*, 15699.

(8) Diao, J.; Qiu, Y.; Liu, S.; Wang, W.; Chen, K.; Li, H.; Yuan, W.; Qu, Y.; Guo, X. Interfacial Engineering of W_2N/WC Heterostructures Derived from Solid-State Synthesis: A Highly Efficient Trifunctional Electrocatalyst for ORR, OER, and Her. *Adv. Mater.* **2020**, *32*, 1905679.

(9) Yang, Y.; Zeng, R.; Xiong, Y.; DiSalvo, F. J.; Abruña, H. D. Cobalt-Based Nitride-Core Oxide-Shell Oxygen Reduction Electrocatalysts. *J. Am. Chem. Soc.* **2019**, *141*, 19241.

(10) Qian, M.; Cheng, X.; Sun, T.; Tian, J.; Isimjan, T. T.; Shi, Z.; Yang, X. Synergistic Catalytic Effect of N-Doped Carbon Embedded with CoFe-rich $CoFe_2O_4$ Clusters as Highly Efficient Catalyst towards Oxygen Reduction. *J. Alloys Compd.* **2020**, *819*, 153015.

(11) Yuan, K.; Lützenkirchen-Hecht, D.; Li, L.; Shuai, L.; Li, Y.; Cao, R.; Qiu, M.; Zhuang, X.; Leung, M. K. H.; Chen, Y.; Scherf, U. Boosting Oxygen Reduction of Single Iron Active Sites via Geometric and Electronic Engineering: Nitrogen and Phosphorus Dual Coordination. *J. Am. Chem. Soc.* **2020**, *142*, 2404.

(12) Guo, M.; Xu, M.; Qu, Y.; Hu, C.; Yan, P.; Isimjan, T. T.; Yang, X. Electronic/Mass Transport Increased Hollow Porous Cu_3P/MoP Nanospheres with Strong Electronic Interaction for Promoting Oxygen Reduction in Zn-Air Batteries. *Appl. Catal. B: Environ.* **2021**, *297*, 120415.

(13) Liu, J.; Xiao, J.; Luo, B.; Tian, E.; Waterhouse, G. I. N. Central Metal and Ligand Effects on Oxygen Electrocatalysis over 3d Transition Metal Single-Atom Catalysts: A Theoretical Investigation. *Chem. Eng. J.* **2022**, *427*, 132038.

(14) Vijayakumar, E.; Ramakrishnan, S.; Sathiskumar, C.; Yoo, D. J.; Balamurugan, J.; Noh, H. S.; Kwon, D.; Kim, Y. H.; Lee, H. MOF-derived CoP-nitrogen-doped carbon@NiFeP Nanoflakes as an Efficient and Durable Electrocatalyst with Multiple Catalytically Active Sites for OER, Her, ORR and Rechargeable Zinc-Air Batteries. *Chem. Eng. J.* **2022**, *428*, 131115.

(15) Zhang, M.; Xu, Y.; Zhang, H.; Duan, Z.; Ren, T.; Wang, Z.; Li, X.; Wang, L.; Wang, H. Synergistic Coupling of P-Doped Pd_4S Nanoparticles with P/S-Co-Doped Reduced Graphene Oxide for Enhanced Alkaline Oxygen Reduction. *Chem. Eng. J.* **2022**, *429*, 132194.

(16) Wang, J.; Zhong, H.; Yang, J.; Li, H.; Tang, P.; Feng, Y.; Li, D. Tuning the Atomic Configuration Environment of MnN_4 Sites by Co Cooperation for Efficient Oxygen Reduction. *J. Energy Chem.* **2023**, *82*, 547.

(17) Qin, Y.; Guo, C.; Ou, Z.; Xu, C.; Lan, Q.; Jin, R.; Liu, Y.; Niu, Y.; Xu, Q.; Si, Y.; Li, H. Regulating Single-Atom Mn Sites by Precisely Axial Pyridinic-Nitrogen Coordination to Stabilize the Oxygen Reduction. *J. Energy Chem.* **2023**, *80*, 542.

(18) Zhu, X.; Amal, R.; Lu, X. N,P Co-Coordinated Manganese Atoms in Mesoporous Carbon for Electrochemical Oxygen Reduction. *Small* **2019**, *15*, 1804524.

(19) Wu, X.; Zhang, Z.; He, C.; Shen, Y.; Wu, X.; Wang, H.; Ma, Z.; Li, Q. Mixed-Valence Cobalt Oxides Bifunctional Electrocatalyst with Rich Oxygen Vacancies for Aqueous Metal-Air Batteries. *Chem. Eng. J.* **2023**, *453*, 139831.

(20) Yang, T.; Xia, Y.; Mao, T.; Ding, Q.; Wang, Z.; Hong, Z.; Han, J.; Peng, D. L.; Yue, G. Phosphorus Vacancies and Heterojunction Interface as Effective Lithium-Peroxide Promoter for Long-Cycle Life Lithium-Oxygen Latteries. *Adv. Funct. Mater.* **2022**, *32*, 2209876.

(21) Cao, Y.; Li, L.; Yu, X.; Tahir, M.; Xiang, Z.; Kong, W.; Lu, Z.; Xing, X.; Song, Y. Engineering Vacancies at the 2d Nanocrystals for Robust Bifunctional Electrocatalysts. *ACS Appl. Mater. Interfaces* **2022**, *14*, 56725.

(22) Douka, A. I.; Xu, Y.; Yang, H.; Zaman, S.; Yan, Y.; Liu, H.; Salam, M. A.; Xia, B. Y. A Zeolitic-Imidazole Frameworks-Derived Interconnected Macroporous Carbon Matrix for Efficient Oxygen Electrocatalysis in Rechargeable Zinc-Air Batteries. *Adv. Mater.* **2020**, *32*, 2002170.

(23) Zhou, F.; Guo, M.; Zhao, N.; Xu, Q.; Zhao, T.; Zhang, W.; Qiu, R. The Effect of Thermal Treatment on the Transformation and Transportation of Arsenic and Cadmium in Soil. *Environ. Sci.* **2024**, *145*, 205.

(24) Zhao, Y.; Shen, Z.; Huo, J.; Cao, X.; Ou, P.; Qu, J.; Nie, X.; Zhang, J.; Wu, M.; Wang, G.; Liu, H. Epoxy-Rich Fe Single Atom Sites Boost Oxygen Reduction Electrocatalysis. *Angew. Chem., Int. Ed.* **2023**, *62*, 202308349.

(25) Wu, L.; Ning, M.; Xing, X.; Wang, Y.; Zhang, F.; Gao, G.; Song, S.; Wang, D.; Yuan, C.; Yu, L.; Bao, J.; Chen, S.; Ren, Z. Boosting Oxygen Evolution Reaction of (Fe,Ni)Ooh via Defect Engineering for Anion Exchange Membrane Water Electrolysis under Industrial Conditions. *Adv. Mater.* **2023**, *35*, 2306097.

(26) Lv, X.; Wan, S.; Mou, T.; Han, X.; Zhang, Y.; Wang, Z.; Tao, X. Atomic-Level Surface Engineering of Nickel Phosphide Nanoarrays for Efficient Electrocatalytic Water Splitting at Large Current Density. *Adv. Funct. Mater.* **2023**, *33*, 2205161.

(27) Yang, Y.; Huang, Y.; Zhou, S.; Liu, Y.; Shi, L.; Isimjan, T. T.; Yang, X. Delicate Surface Vacancies Engineering of Ru Doped MOF-derived Ni-NiO@C Hollow Microsphere Superstructure to Achieve Outstanding Hydrogen Oxidation Performance. *J. Energy Chem.* **2022**, *72*, 395.

(28) Arshad, A.; Yun, S.; Shi, J.; Sun, M.; Zafar, N.; Hagfeldt, A. N-Coordinated Bimetallic Defect-Rich Nanocarbons as Highly Efficient Electrocatalysts in Advanced Energy Conversion Applications. *Chem. Eng. J.* **2022**, *435*, 134913.

(29) Mantry, S. P.; Mohapatra, B. D.; Behera, N.; Mishra, P.; Parhi, P.; Varadwaj, K. S. K. Potentiostatic Regeneration of Oxygen Reduction Activity in MnO_x@Graphene Hybrid Nanostructures. *Electrochim. Acta* **2019**, *325*, 134947.

(30) Zhou, Y.; Lu, R.; Tao, X.; Qiu, Z.; Chen, G.; Yang, J.; Zhao, Y.; Feng, X.; Müllen, K. Boosting Oxygen Electrocatalytic Activity of Fe-

N-C Catalysts by Phosphorus Incorporation. *J. Am. Chem. Soc.* **2023**, *145*, 3647.

(31) Li, Z.; Ji, S.; Liu, H.; Xu, C.; Guo, C.; Lu, X.; Sun, H.; Dou, S.; Xin, S.; Horton, J. H.; He, C. Constructing Asymmetrical Coordination Microenvironment with Phosphorus-Incorporated Nitrogen-Doped Carbon to Boost Bifunctional Oxygen Electrocatalytic Activity. *Adv. Funct. Mater.* **2024**, *34*, 2314444.

(32) Li, S.; Wang, R.; Yang, X.; Wu, J.; Meng, H.; Xu, H.; Ren, Z. Binary Metal Phosphides with MoP and FeP Embedded in P,N-Doped Graphitic Carbon as Electrocatalysts for Oxygen Reduction. *ACS Sustainable Chem. Eng.* **2019**, *7*, 11872.

(33) Xu, Q.; Peng, X.; Zhu, Z.; Luo, K.; Liu, Y.; Yuan, D. Co_2P Nanoparticles Supported on Cobalt-Embedded N-Doped Carbon Materials as a Bifunctional Electrocatalyst for Rechargeable Zn-Air Batteries. *Int. J. Hydrogen Energy* **2022**, *47*, 16518.

(34) Xu, Y.; Wang, R.; Wang, J.; Zhang, Y.; Jiao, T. Encapsulation of Fe-CoP with P, N-co-doped porous carbon matrix as a Multifunctional Catalyst for Wide Electrochemical Applications. *J. Energy Chem.* **2022**, *71*, 36.

(35) Zhao, M.; Liu, H.; Zhang, H.; Chen, W.; Sun, H.; Wang, Z.; Zhang, B.; Song, L.; Yang, Y.; Ma, C.; Han, Y.; Huang, W. A Ph-Universal ORR Catalyst with Single-Atom Iron Sites Derived from a Double-Layer Mof for Superior Flexible Quasi-Solid-State Rechargeable Zn-Air Batteries. *Energy Environ. Sci.* **2021**, *14*, 6455.

(36) Huang, J.; Xu, X.; Yan, Y.; Zheng, Y.; Yao, Y.; Li, Z.; Yan, Y.; Hui, K. N.; Zou, J.; Liu, M. Facile Microwave Synthesis of Kilogram-Scale Electrocatalysts with Nanocarbons Bridged Cobalt Active Sites for Enhanced Oxygen Electrocatalysis. *Adv. Energy Mater.* **2025**, *15*, 2500360.

(37) Xiao, M.; Xing, Z.; Jin, Z.; Liu, C.; Ge, J.; Zhu, J.; Wang, Y.; Zhao, X.; Chen, Z. Preferentially Engineering FeN_4 Edge Sites onto Graphitic Nanosheets for Highly Active and Durable Oxygen Electrocatalysis in Rechargeable Zn-Air Batteries. *Adv. Mater.* **2020**, *32*, 2004900.

(38) Liang, L.; Jin, H.; Zhou, H.; Liu, B.; Hu, C.; Chen, D.; Wang, Z.; Hu, Z.; Zhao, Y.; Li, H.-W.; He, D.; Mu, S. Cobalt Single Atom Site Isolated Pt Nanoparticles for Efficient ORR and Her in Acid Media. *Nano Energy* **2021**, *88*, 106221.

(39) Niu, S.; Li, S.; Du, Y.; Han, X.; Xu, P. How to Reliably Report the Overpotential of an Electrocatalyst. *Acs Energy Lett.* **2020**, *5*, 1083.

(40) Garsany, Y.; Baturina, O. A.; Swider-Lyons, K. E.; Kocha, S. S. Experimental Methods for Quantifying the Activity of Platinum Electrocatalysts for the Oxygen Reduction Reaction. *Anal. Chem.* **2010**, *82*, 6321.

(41) Xie, Z.; Li, Q.; Peng, X.; Wang, X.; Guo, L.; Zhang, X.; Lu, Z.; Yang, X.; Yu, X.; Li, L. Promoting Interfacial Charge Transfer by B/N Co-Doping Enables Efficient ORR Catalysis of Carbon-Encapsulated Fe_2N. *J. Mater. Chem. A* **2022**, *10*, 4191.

(42) Zhong, G.; Xu, S.; Liu, L.; Zheng, C. Z.; Dou, J.; Wang, F.; Fu, X.; Liao, W.; Wang, H. Effect of Experimental Operations on the Limiting Current Density of Oxygen Reduction Reaction Evaluated by Rotating-Disk Electrode. *ChemElectroChem.* **2020**, *7*, 1107−1114.

(43) Paudel, D. R.; Pan, U. N.; Ghising, R. B.; Dhakal, P. P.; Dinh, V. A.; Wang, H.; Kim, N. H.; Lee, J. H. Interface Modulation Induced by the 1t Co-Ws_2 Shell Nanosheet Layer at the Metallic $Nite_2$/Ni Core-Nanoskeleton: Glib Electrode-Kinetics for Her, OER, and ORR. *Nano Energy* **2022**, *102*, 107712.

(44) Qian, M.; Xu, M.; Zhou, S.; Tian, J.; Isimjan, T. T.; Shi, Z.; Yang, X. Template Synthesis of Two-Dimensional Ternary Nickel-Cobalt-Nitrogen Co-Doped Porous Carbon Film: Promoting the Conductivity and More Active Sites for Oxygen Reduction. *J. Colloid Interface Sci.* **2020**, *564*, 276.

(45) Chen, M.; Zhang, Y.; Wang, R.; Zhang, B.; Song, B.; Guan, Y.; Li, S.; Xu, P. Surface Reconstruction of Se-Doped NiS_2 Enables High-Efficiency Oxygen Evolution Reaction. *J. Energy Chem.* **2023**, *84*, 173.

(46) Ahsan, M. A.; He, T.; Eid, K.; Abdullah, A. M.; Curry, M. L.; Du, A.; Santiago, A. R. P.; Echegoyen, L.; Noveron, J. C. Tuning the Intermolecular Electron Transfer of Low-Dimensional and Metal-Free BCN/C_{60} Electrocatalysts via Interfacial Defects for Efficient Hydrogen and Oxygen Electrochemistry. *J. Am. Chem. Soc.* **2021**, *143*, 1203.

(47) Kong, F.; Cui, X.; Huang, Y.; Yao, H.; Chen, Y.; Tian, H.; Meng, G.; Chen, C.; Chang, Z.; Shi, J. N-Doped Carbon Electrocatalyst: Marked ORR Activity in Acidic Media without the Contribution from Metal Sites? *Angew. Chem., Int. Ed.* **2022**, *61*, 202116290.

(48) Zhang, M.; Li, H.; Chen, J.; Ma, F.-X.; Zhen, L.; Wen, Z.; Xu, C.-Y. A Low-Cost, Durable Bifunctional Electrocatalyst Containing Atomic Co and Pt Species for Flow Alkali-Al/Acid Hybrid Fuel Cell and Zn-Air Battery. *Adv. Funct. Mater.* **2023**, *33*, 2303189.

(49) Maiti, K.; Balamurugan, J.; Gautam, J.; Kim, N. H.; Lee, J. H. Hierarchical Flowerlike Highly Synergistic Three-Dimensional Iron Tungsten Oxide Nanostructure-Anchored Nitrogen-Doped Graphene as an Efficient and Durable Electrocatalyst for Oxygen Reduction Reaction. *ACS Appl. Mater. Interfaces* **2018**, *10*, 32220.

(50) Luo, X.; Zhao, H.; Tan, X.; Lin, S.; Yu, K.; Mu, X.; Tao, Z.; Ji, P.; Mu, S. Fe-S Dually Modulated Adsorbate Evolution and Lattice Oxygen Compatible Mechanism for Water Oxidation. *Nat. Commun.* **2024**, *15*, 8293.

(51) Xue, D.; Yuan, Y.; Yu, Y.; Xu, S.; Wei, Y.; Zhang, J.; Guo, H.; Shao, M.; Zhang, J.-N. Spin Occupancy Regulation of the Pt d-Orbital for a Robust Low-Pt Catalyst towards Oxygen Reduction. *Nat. Commun.* **2024**, *15*, 5990.

(52) Niu, H.; Huang, L.; Qin, Y.; Qi, R.; Mei, B.; Wu, D.; Li, F.-M.; You, B.; Li, Q.; Yao, Y.; Wang, Z.; Yao, T.; Ding, S.; Guo, W.; Chen, Y.; Su, Y.; Song, F.; Xia, B. Y. Hydrogen Peroxide Spillover on Platinum-Iron Hybrid Electrocatalyst for Stable Oxygen Reduction. *J. Am. Chem. Soc.* **2024**, *146*, 22650.

(53) Ji, S. G.; Kim, M. M.; Han, M. H.; Cho, J.; Son, Y.; Kim, Y. Y.; Jeong, J.; Kim, Z. H.; Chae, K. H.; Oh, H.-S.; Kim, H.; Choi, C. H. Alkali Metal Cations Act as Homogeneous Cocatalysts for the Oxygen Reduction Reaction in Aqueous Electrolytes. *Nat. Catal.* **2024**, *7*, 1330.

(54) Chen, Y.; Zhang, S.; Jung, J. C.-Y.; Zhang, J. Carbons as Low-Platinum Catalyst Supports and Non-Noble Catalysts for Polymer Electrolyte Fuel Cells. *Prog. Energy Combust. Sci.* **2023**, *98*, 101101.

(55) Wang, L.; Gennari, M.; Reinhard, F. G. C.; Gutiérrez, J.; Morozan, A.; Philouze, C.; Demeshko, S.; Artero, V.; Meyer, F.; Visser, S. P. d.; Duboc, C. A Non-Heme Diiron Complex for Electrocatalytic Reduction of Dioxygen: Tuning the Selectivity through Electron Delivery. *J. Am. Chem. Soc.* **2019**, *141*, 8244.

(56) Luo, X.; Wu, W.; Wang, Y.; Li, Y.; Ye, J.; Wang, H.; Jiang, Q.; Zhou, Z.; Li, Y. C.; Wang, Y.; Sun, S. Relay Catalysis of Multi-Sites Promotes Oxygen Reduction Reaction. *Adv. Funct. Mater.* **2023**, *33*, 2215021.

(57) Liu, H.; Guan, J.; Yang, S.; Yu, Y.; Shao, R.; Zhang, Z.; Dou, M.; Wang, F.; Xu, Q. Metal-Organic Framework-Derived Co_2P Nanoparticle/Multi-Doped Porous Carbon as a Trifunctional Electrocatalyst. *Adv. Mater.* **2020**, *32*, 2003649.

(58) Chao, G.; Zhang, Y.; Zhang, L.; Zong, W.; Zhang, N.; Xue, T.; Fan, W.; Liu, T.; Xie, Y. Nitrogen-Coordinated Single-Atom Catalysts with Manganese and Cobalt Sites for Acidic Oxygen Reduction. *J. Mater. Chem. A* **2022**, *10*, 5930.

(59) Duan, J.; Chen, S.; Ortíz-Ledón, C. A.; Jaroniec, M.; Qiao, S.-Z. Phosphorus Vacancies That Boost Electrocatalytic Hydrogen Evolution by Two Orders of Magnitude. *Angew. Chem., Int. Ed.* **2020**, *59*, 8181.